

Investigation of the bond properties between hybrid fiber-reinforced concrete and BFRP bars after exposure to high temperature

✉ Z. Liu^a, H. Liu^a, W. Xu^b, B. Liu^b, Y. Zhong^c, J. Geng^d, G. Liu^d ✉

a. College of Civil and Architectural Engineering, Liaoning University of Technology, (Jinzhou, China)
b. School of Architecture, Tianjin University, (Tianjin, China)
c. Centre for Infrastructural Monitoring and Protection, School of Civil and Mechanical Engineering, Curtin University, (Bentley, Australia)
d. School of Civil Engineering, NingboTech University, (Ningbo, China)
✉: liugenjin@163.com

Received 06 August 2023
Accepted 11 December 2023
Available on line 25 March 2024

ABSTRACT: This research investigated the bond properties at high temperatures and with hybrid fiber addition between basalt fiber reinforced polymer (BFRP) bars and hybrid fiber-reinforced concrete (HFRC). The tensile strength and appearance morphology of BFRP bars were analyzed. Used scanning electron microscopy (SEM) to examine the microscopic morphology and used the bond-slip constitutive model to fit the bond-slip curves. When BFRP bars after exposed to 300 °C, their tensile strength dropped by 42%. With the increasing temperature, the bond strength and stiffness of normal concrete (NC) specimens decreased by 27.3 % and 67.5 %, respectively, while HFRC specimens decreased by 20.8 % and 55 %, respectively. Hybrid fibers increased the bond strength and stiffness of HFRC specimens by 27.1 % and 49.1 %, respectively. The best fitting models were the Malvar model and the Continuous Curve model.

KEY WORDS: High temperature; BFRP bar; Hybrid fiber-reinforced concrete; Microscopic morphology; Bond properties.

Citation/Citar como: Liu Z, Liu H, Xu W, Liu B, Zhong Y, Geng J, Liu G. 2024. Investigation of the bond properties between hybrid fiber-reinforced concrete and BFRP bars after exposure to high temperature. *Mater. Construcc.* 74(353):e334. <https://doi.org/10.3989/mc.2024.361123>.

RESUMEN: *Investigación de las propiedades de adherencia entre el hormigón reforzado con fibras híbridas y las barras BFRP tras la exposición a altas temperaturas.* Esta investigación evaluó las propiedades de adherencia a altas temperaturas y con adición de fibra híbrida entre barras de polímero reforzado con fibra de basalto (BFRP) y hormigón reforzado con fibra híbrida (HFRC). Se analizaron la resistencia a la tracción y la morfología del aspecto de las barras de BFRP. Se utilizó microscopía electrónica de barrido (SEM) para examinar la morfología microscópica y se utilizó el modelo constitutivo de adherencia-deslizamiento para ajustar las curvas de adherencia-deslizamiento. Cuando las barras de BFRP se expusieron a 300 °C, su resistencia a la tracción disminuyó un 42%. Con el aumento de la temperatura, la resistencia de adherencia y la rigidez de los especímenes de hormigón normal (NC) disminuyeron un 27,3% y un 67,5%, respectivamente, mientras que los especímenes HFRC disminuyeron un 20,8% y un 55%, respectivamente. Las fibras híbridas aumentaron la resistencia de adherencia y la rigidez de las probetas HFRC en un 27,1 % y un 49,1 %, respectivamente. Los modelos que mejor se ajustaron fueron el modelo de Malvar y el modelo de curva continua.

PALABRAS CLAVE: Alta temperatura; Barra de PRFB; Hormigón reforzado con fibra híbrida; Morfología microscópica; Propiedades adhesivas.

Copyright: ©2024 CSIC. This is an open-access article distributed under the terms of the Creative Commons Attribution 4.0 International (CC BY 4.0) License.

1. INTRODUCTION

Fire and high temperature can cause thermal stress and rapid evaporation of water in building structures, which can increase the internal pore pressure and lead to irreversible, permanent damage such as explosion and spalling (1, 2). To minimize the damage, the building structures after fire exposure need to have sufficient strength, stiffness, and stability (3, 4). Therefore, enhancing the high-temperature resistance of concrete structures has become a research hotspot.

Numerous studies had demonstrated that incorporating fiber materials into concrete could reduce the pore pressure and prevent the concrete from spalling under high temperatures. Moreover, the mechanical properties after high temperatures could be enhanced effectively by fiber reinforcement (5-7). The improving effect of single fiber was limited, whereas HFRC, which combined two types of fibers, showed a significantly better performance than single fiber reinforced concrete (8-10). This was due to the positive interaction between different fibers, particularly between high elastic modulus fibers and low elastic modulus fibers, which significantly enhanced the durability and mechanical properties (11).

Basalt fiber (BF) had properties such as light weight, fatigue resistance, environmental friendliness, high-temperature resistance, and corrosion resistance (12, 13). It had a better performance-to-price ratio than carbon fiber, and compared with glass fiber, it had higher strength and elastic modulus (14). The wide distribution of basalt also enhanced the development potential of BF. Niaki *et al.* (15) examined the BF and nanoclay-reinforced polymer concrete under various temperatures. Their results indicated that BF enhanced the thermal stability of concrete. Ren *et al.* (16) evaluated the basalt fiber reinforced concrete (BFRC) after high temperature. They found that the ultrasonic pulse velocity of BFRC reduced as the temperature increased, while the strain rate, impact toughness, and dynamic strength rose as the impact velocity increased at a constant temperature. Therefore, BF could enhance the residual strength, deformation capacity, and energy absorption capacity.

Plant fibers also received more attention from researchers in the context of green environmental protection and sustainable development. Cellulose fiber (CF) was the most prevalent material, with a wide distribution in nature, degradability, a low processing cost, non-toxicity, and high recyclability (17). It was a low-carbon environmental protection material and had a wide application in concrete production. The good hydrophilicity of CF could facilitate cement hydration and internal curing during concrete curing (18, 19). Therefore, the mechanical properties could improve. Hisseine *et al.* (20) performed a multi-scale evaluation of CF cement-based materials using a combination of macro and micro research methods. They found that the CF increased the de-

mand for water-reducing agents and enhanced the macroscopic mechanical properties and that the energy absorption capacity of cement paste was proportional to the fiber content. Microstructural studies revealed a strong bond of CF. Due to the good hydrophilicity and large specific surface area of the CF, the CH group and the calcium silicate hydrate (C-S-H) gel attached to the CF, which enhanced the hydration degree of the cement.

The safety of reinforced concrete structures was endangered by steel bar corrosion, and maintaining existing buildings due to steel bar corrosion required much manpower and financial resources. One of the best ways to address this durability issue was with fiber reinforced polymer (FRP) bars (21, 22). However, its matrix was polymer resin material, which softened and decomposed after exposure to high temperatures, leading to poor fire resistance. Therefore, it was mainly applied in structures without fire resistance requirements (23). Hence, studying its bond properties after exposure to fire and high temperature was imperative, which affected the popularity and application of FRP-reinforced concrete structures. The influence of high temperature on the bond properties of GFRP bars was investigated by Hamzeh *et al.* (24). They found that increased temperature caused the bond stiffness to decrease. They also found that the most important factor was the glass transition temperature, and determined the critical temperature of different types of GFRP bars to be 100 °C ~ 140 °C. The bond properties of BFRP bars, CFRP bars, and GFRP bars under temperature were investigated by Hamad *et al.* (25). The bond strength of CFRP bars was the highest among the three types, followed by GFRP bars, and then BFRP bars. The bond strength of BFRP bars, GFRP bars, CFRP bars, and steel bars was reduced by 79.9 %, 79.2 %, 81.5 %, and 27.2 % respectively after exposure to 325 °C. The bond properties of BFRP bars under different temperatures were studied by Li *et al.* (26). They compared the bond-slip curve of BFRP bars with that of steel bars and analyzed the effect of temperature and types of bars on the bond properties. They observed that the bond-slip curve of BFRP bars was similar to that of steel bars, but the bond strength and stiffness of BFRP bars decreased with increased temperature. The bond strength was reduced by 2.5 % ~ 14.2 % at temperatures 70 °C ~ 220 °C and by 32 % when the temperature was 270 °C. However, they noted the residual bond strength which was only 12.2 % ~ 23.1 % at a temperature of 350 °C. They concluded that the bond strength of GFRP bars was lower than BFRP bars under different temperature conditions.

Many factors would influence the mechanical properties of concrete structures after heating, such as temperature, size effect, external load, and cooling method after heating (27). However, the bond properties between FRP bars and concrete after exposure to high temperatures were not well studied, and the

influence of temperature on residual bond strength was uncertain. This effect was important for assessing the fire resistance of structures. Therefore, this research examined the effects of high temperatures and the incorporation of hybrid fiber of BF and CF on the bond properties between BFRP bars and concrete. Compared and analyzed the appearance morphology and tensile strength of BFRP bars after being cooled to 20 °C following high-temperature treatment at different temperatures. Additionally, the failure mode, bond stiffness, bond strength, and bond-slip curves of pull-out specimens after being cooled to 20 °C following high-temperature treatment were also analyzed. The residual bond strength of the specimens was fitted with a polynomial. The concrete in the bonding interface of bars was analyzed by SEM. The bond-slip curve was fitted with the existing bond-slip constitutive models. This research aimed to provide experimental evidence for the engineering application of FRP-reinforced concrete structures.

2. MATERIALS AND METHODS

2.1. Materials

P.O 42.5 normal Portland cement from Bohai Cement (Huludao) Co., Ltd. was used in this test. The local granite gravel was used as the coarse aggregate which had a continuous gradation in the 5-20 mm particle size range. The local ordinary river sand in Jinzhou was used as fine aggregate which had a fineness modulus of 2.7. Table 1 and Table 2 show the physical properties of coarse and fine aggregate, respectively. The granulometry curves of aggregates from the tests according to GB/T 14685-2022 (28) and GB/T 14684-2022 (29) are shown in Figure 1. Urban tap water from Jinzhou City Tap Water Plant was used as the water. The BF and CF were from Jiangsu Tianlong Continuous Basalt Fibre Co., Ltd. and Taian Tongban

FIBER Co., Ltd, respectively. The BFRP bars were 12 mm in diameter and 500 mm in length, with a sand-coated ribbed surface treatment, from Jiangsu Green Material Valley New Material Technology Development Co., Ltd. Table 3 and Table 4 show the material properties of fibers and BFRP bars, respectively. Figure 2 shows the appearance morphology of fibers and BFRP bars.

The concrete mixture proportion was designed according to JGJ 55-2011 (30). The mix proportion of benchmark concrete was mass (cement): mass (sand): mass (coarse aggregate) = 1: 1.46: 2.06, and the water-binder ratio was 0.48. The volume content of BF and CF was set to be 0.15 % and 0.2 % of the concrete volume, respectively, based on existing research (31, 32). The target temperature was set to be 20 °C, 100 °C, 200 °C, 300 °C, 400 °C and 500 °C. The main objective was to investigate the effect of the addition of BF and CF on the bond properties. Therefore, the change in fiber content was not considered.

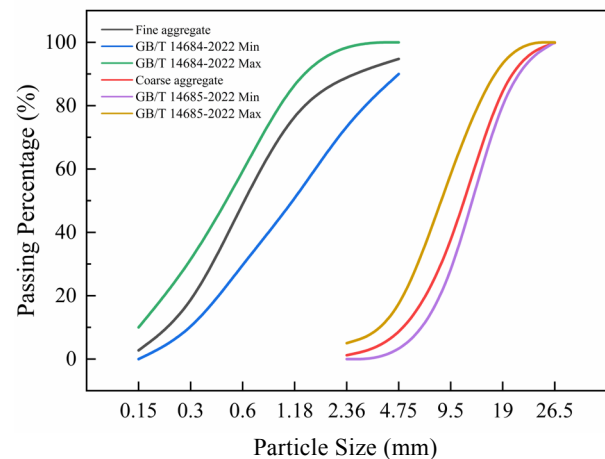


FIGURE 1. Granulometry curves of aggregate.

TABLE 1. Physical property of coarse aggregate.

Apparent density (kg/m ³)	Bulk density (kg/m ³)	Mud content (%)	Crushing index (%)	Content of needle and flake particles (%)
2680	1630	0.3	8.9	3.7

TABLE 2. Physical property of fine aggregate.

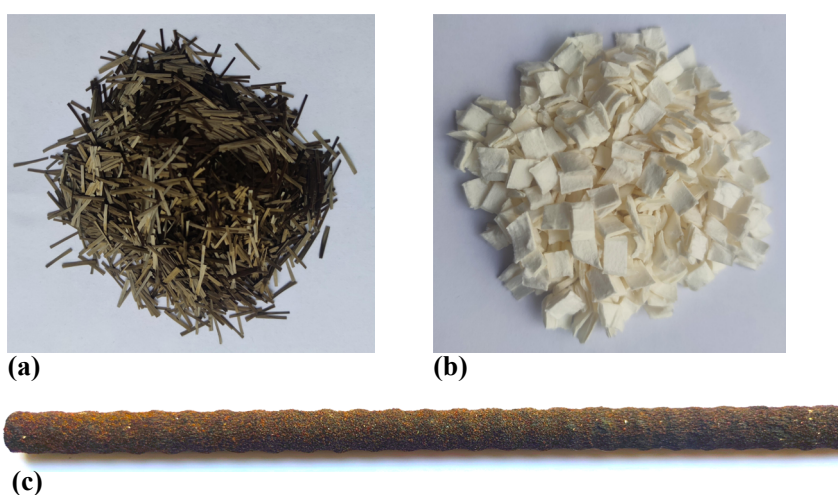
Apparent density (kg/m ³)	Bulk density (kg/m ³)	Water absorption (%)	Water content (%)	Mud content (%)	Crushing index (%)
2541	1567	1.3	0.8	1.8	10.4

TABLE 3. Material properties of fibers.

Fiber type	Length (mm)	Diameter (μm)	Density (g/cm^3)	Elastic modulus (GPa)	Tensile strength (MPa)
BF	12	16	2.6~2.8	90~110	4150~4800
CF	2.1	17.9	1.2	8~10	500~1000

TABLE 4. Material properties of BFRP bar.

Cross section area (mm^2)	Tensile strength (MPa)	Elastic modulus (GPa)	Density (g/cm^3)	Elongation at break (%)
113.10	1216	52.5	2.02	2.3

**FIGURE 2.** Appearance morphology of fiber and BFRP bar. (a) BF; (b) CF; (c) BFRP bar.

2.2. Design of pull-out specimens

Table 5 shows the specimen groups. This test consisted of 8 groups of specimens, with 3 specimens in each group. The specimen number was represented

by a combination of letters and numbers, where HN and HF respectively represented NC and HFRC, and the number represented the target temperature. For example, HF300 referred to specimens of HFRC after exposure to 300 °C.

TABLE 5. Specimen groups used in pull-out test.

Specimens number	Type of concrete	BF volume content (%)	CF volume content (%)	Target temperature (°C)
HN20	NC	0	0	20
HN100	NC	0	0	100
HN200	NC	0	0	200
HN300	NC	0	0	300
HF20	HFRC	0.15	0.2	20
HF100	HFRC	0.15	0.2	100
HF200	HFRC	0.15	0.2	200
HF300	HFRC	0.15	0.2	300

The specimen with a 150 mm side length, following the guidelines of ACI440.3R-12 (33). The center of the cube specimen was vertically penetrated by the BFRP bar. Based on ACI 440.1R-06 (34) and the findings of Eduarda et al. (35), the bond length was set to be 5d (60 mm), and the bond area was located in the upper portion of the concrete. The bond anchorage length was precisely controlled by sleeving a 90 mm ceramic sleeve in the unbonded area. The tape was used to attach the ceramic sleeve and the BFRP bar, and epoxy resin for 1 mm sealed both ends to avoid mortar intrusion during the casting process. The free end had a 20 mm length reserved for measuring the relative slip. The loading end was anchored by a galvanized steel tube with a 100 mm length to prevent its shear failure during the test. The specimens underwent curing at 23 ± 2 °C and 95 % humidity for 28 days after casting. Figure 3 shows the pull-out specimen.

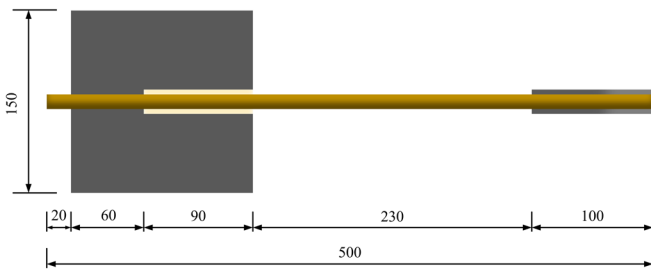


FIGURE 3. Diagram of pull-out specimen.

2.3. Test setup

The SX2-12-10 box resistance furnace was used as the heating device, with a 10 °C/min heating rate and a 1200 °C maximum temperature. A high temperature protection treatment was applied to the exposed BFRP bars by wrapping them with a combination of fire retardant coating and fireproof asbestos before heating. After reaching the target temperature (100 °C, 200 °C, 300 °C, 400 °C, 500 °C), the specimens were maintained at constant temperature for 5h in the resistance furnace and then cooled to 20 °C. The temperature-time curves in the furnace were measured by the K-type thermocouple inside the resistance furnace, as shown in Figure 4. Before the formal test, conducted a pre-test to measure the temperature-time curve inside the specimen using a K-type thermocouple embedded in the BFRP bar bond area, as shown in Figure 5. After being held at a constant temperature for 5 hours, the internal temperature of each pull-out specimen reached the target temperature basically. At target temperatures of 100 °C, 200 °C, 300 °C, 400 °C, and 500 °C, respectively, HN specimens had an average heating rate of 0.36 °C/min, 0.62 °C/min, 0.95 °C/min, 1.35 °C/min,

and 1.82 °C/min, the average heating rates of HF specimens were 0.35 °C/min, 0.60 °C/min, 0.94 °C/min, 1.39 °C/min, and 2.12 °C/min. The internal heating rate of the specimens increased as the target temperature increased, but it was lower than that of the high-temperature furnace. Furthermore, no concrete spalling occurred.

The central pull-out test was applied to the pull-out specimens in accordance with GB/T 30022-2013 (36). Before the test, the specimens should be placed in the reaction force test device which was shown in Figure 6(a). The device was primarily composed of two thick backing plates, a center retainer bar, and four long retainer bars. Adjusted the nuts of the four long retainer bars in the reaction force test device to make the bottom surface of the pull-out specimen tightly adhere to the steel plate to avoid eccentric loading. After adjusting the pull-out specimen, using the upper and lower fixtures of the WDW-300 KN electro-hydraulic servo testing machine to clamp the center retainer bar of the reaction force test device and the steel tube of the pull-out specimen respectively, as shown in Figure 6(b). A linear variable displacement transducer (LVDT) was placed between the free end and the end of the center retainer bar of the reaction force test device to measure the slip value. Afterward, it was loaded at a rate of 1 mm/min, which was controlled by displacement.

The average bond stress τ for each group of specimens was calculated according to ASTM D7913/D7913M-14 (37). The formula is shown in Equation [1]:

$$\tau = \frac{P}{\pi d l_a} \quad [1]$$

Where τ was the average bond stress between the BFRP bar and concrete, MPa; P was the ultimate failure load of the specimen, N; d was the diameter of the BFRP bar, mm; l_a was the bond anchorage length of the BFRP bar, mm.

The TESCAN MIRA LMS and ZEISS Sigma 300 scanning electron microscopes were used to observe the internal microstructure of concrete. The SEM samples

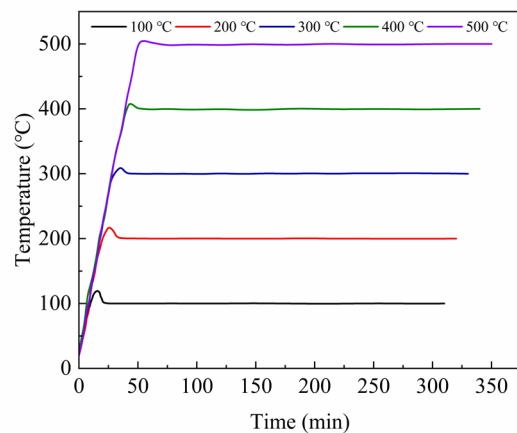


FIGURE 4. Temperature-time curve in a furnace.

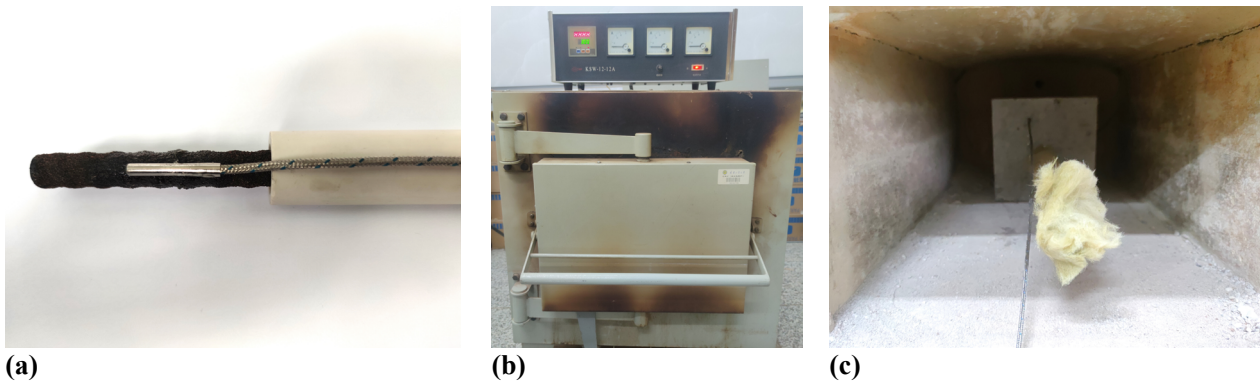


FIGURE 5. Measurement of the internal temperature of the specimen. (a) Paste of K-type thermocouple; (b) SX2-12-10 box resistance furnace; (c) Pull-out specimens being prepared for high-temperature treatment.

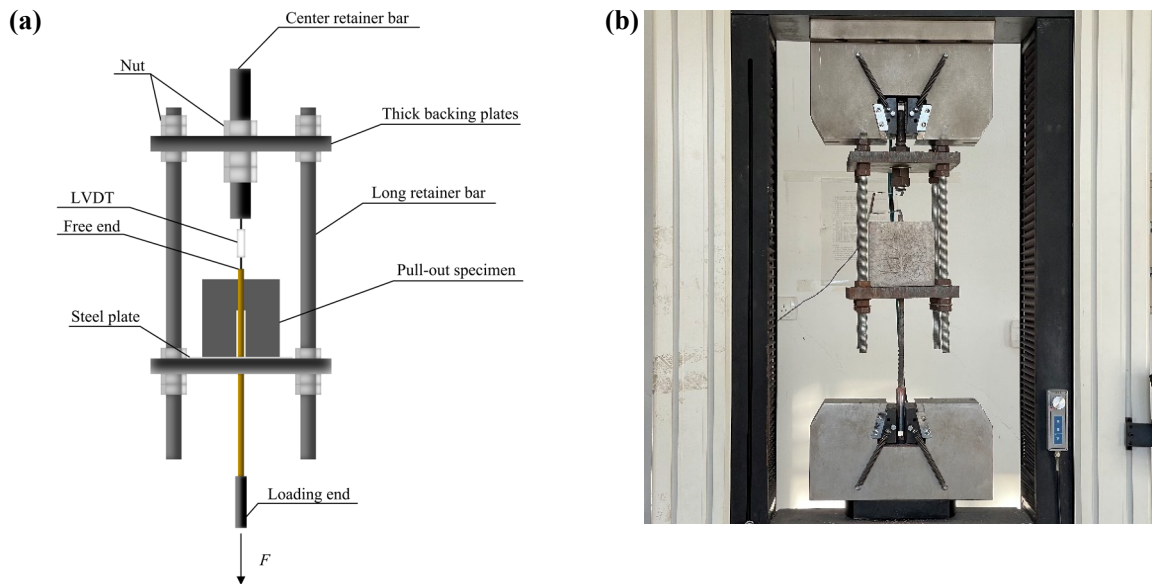


FIGURE 6. The pull-out test setup. (a) Detail of reaction force test device; (b) Reaction force test device and testing machine.

were taken from the concrete in the bonding interface.

3. RESULTS AND DISCUSSION

3.1. Appearance morphology and tensile strength of bfrp bars after exposure to high temperatures

Figure 7 shows the appearance morphology changes of BFRP bars with the increase in temperature. Significant changes in surface color were caused by temperature increase. Before 200 °C, the surface color remained almost unchanged, and only a few sand particles fell off. The surface color turned to carbon black after 300 °C, and all the sand particles came off. The matrix resin of the BFRP bars began to decompose after reaching the melting point at 400 °C, and a golden brown color appeared. The fibers of the bars

became loose after 500 °C, and the matrix resin completely decomposed and lost its viscosity. The severe decomposition of the matrix resin after 500 °C eliminated the tensile strength, which prevented the subsequent pull-out test from being conducted. Hence, the temperature range of the tensile test in this research was from 20 °C to 400 °C.

Table 6 shows the tensile test results. The BFRP bar had glass transition temperature (T_g) and thermal decomposition temperature (T_d) in a high-temperature environment (38). With rising temperatures, the tensile strength dropped. When exposed to 100 °C, the tensile strength was 1.6% lower than when it was at 20 °C. The tensile strength decreased by 6.3 % after exposure to 200 °C, where the BFRP bar matrix resin reached the T_g . The tensile strength partially recovered after the matrix resin solidified upon cooling to 20 °C. The tensile strength dropped by 41.8 % at 300 °C and reached only 13.2 % of its initial value

at 400 °C. This was due to the resin matrix reaching the T_g at 300 °C and undergoing irreversible oxidation and decomposition after being heated at a constant temperature for 5h. The tensile strengths were not significantly influenced by temperatures below 300 °C compared to it at 20 °C. However, the tensile strength declined rapidly at 300 °C. The low resistance of FRP bars to high temperatures was mainly attributed to T_g and T_d of the resin. Only the specimens exposed to

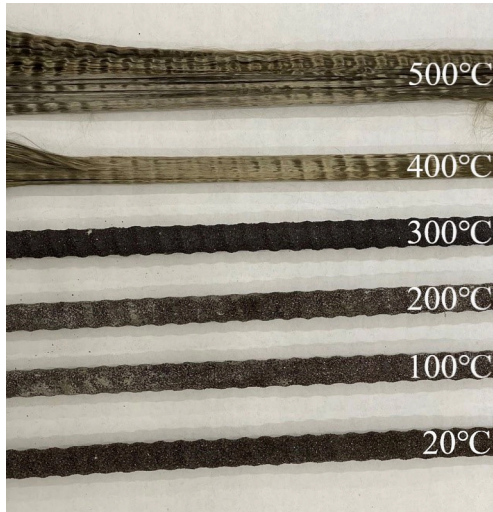


FIGURE 7. Appearance morphology changes of BFRP bars after high temperature.

TABLE 6. Tensile strength of BFRP bar.

Temperature (°C)	20	100	200	300	400
Tensile strength (MPa)	1216	1197	1140	708	161

temperatures of 20 °C, 100 °C, 200 °C, and 300 °C conducted pull-out tests, as the tensile strength of the bar was severely deteriorated at 400 °C.

3.2. Microstructure of the concrete

Figures 8(a) and 8(b) show the SEM images of HF specimens at 20 °C. Figure 8(a) shows that the concrete mainly contained C-S-H gel, acicular ettringite (AFT), and hexagonal $\text{Ca}(\text{OH})_2$ (CH). The microstructure was dense, and the pores were less. The aggregate and the solidified cementitious material were bonded together to form a uniform and dense continuous phase, which gave the cement paste a strong bond performance. Figure 8(b) shows that the surface of BF was covered by dense hydration products (C-S-H gel or CH crystal group). This indicated that there were good bonds in fiber and could be

well embedded into the concrete matrix. This strong bond could enhance the force transfer of fiber, reduce internal damage, and then improve the bond properties. Figures 8(c) and 8(d) show that there were many voids in the HN specimen, and there was no substance inside the voids. However, the voids in the HF specimen were filled with a large amount of hydration products, which divided the large voids into small ones. The hydration products at the bonding interface in the HF specimen were significantly more than those in the HN specimen.

Figures 8(e) and 8(f) show the SEM images of HF and HN specimens at 200 °C, respectively. A lot of capillary water, free water, and bound water evaporated from the concrete at 200 °C, creating pores in the previously uniform and dense continuous medium. BF filled the pores and was slightly worn but not broken in HF, as shown in Figure 8(f). The gaps and micro-cracks in the concrete could be bridged. The secondary hydration reaction on the surface of BF produced many C-S-H gels and fine spherical particles that adhered to the fiber surface, which enhanced the mechanical interaction of fiber, and restrained the expansion of microcracks. The high thermal conductivity of BF could effectively transfer temperature and reduce the temperature gradient inside and outside the concrete.

Figure 8 (g) ~ (h) show the SEM images of HF specimens after exposure to 300 °C. At 300 °C, the CF melted, and pores formed inside the matrix. Although the pores caused porosity to increase, they also provided a release channel for pore pressure and uneven thermal expansion stress. The decomposition of CH reduced the bond between cementitious materials and aggregates, resulting in a loose and porous internal structure of concrete. The surface of BF became smooth and had tiny cracks, indicating that the interface bonding force was weakened and some debonding occurred between fiber and matrix. Fiber fracture was the primary failure mode of BF, indicating that BF and matrix bear stress together before fracture. The cracks between BF and matrix further extended and connected with the pores left by the melting of CF to form the penetrating cracks.

3.3. Failure mode of pull-out specimens

Figure 9 illustrates the failure modes, which were classified as splitting failure, pull-out failure, and pull-out splitting failure.

In the case of splitting failure, a slight slip occurred on the loading end at the onset of the test loading, whereas the free end remained stable. As the load increased, the slip at the loading end increased, and the free end also began to slip. Splitting failure of the concrete occurred when the tangential tensile stress induced by the radial force exceeded the ultimate tensile strength of the concrete, resulting in an apparent brittle failure.

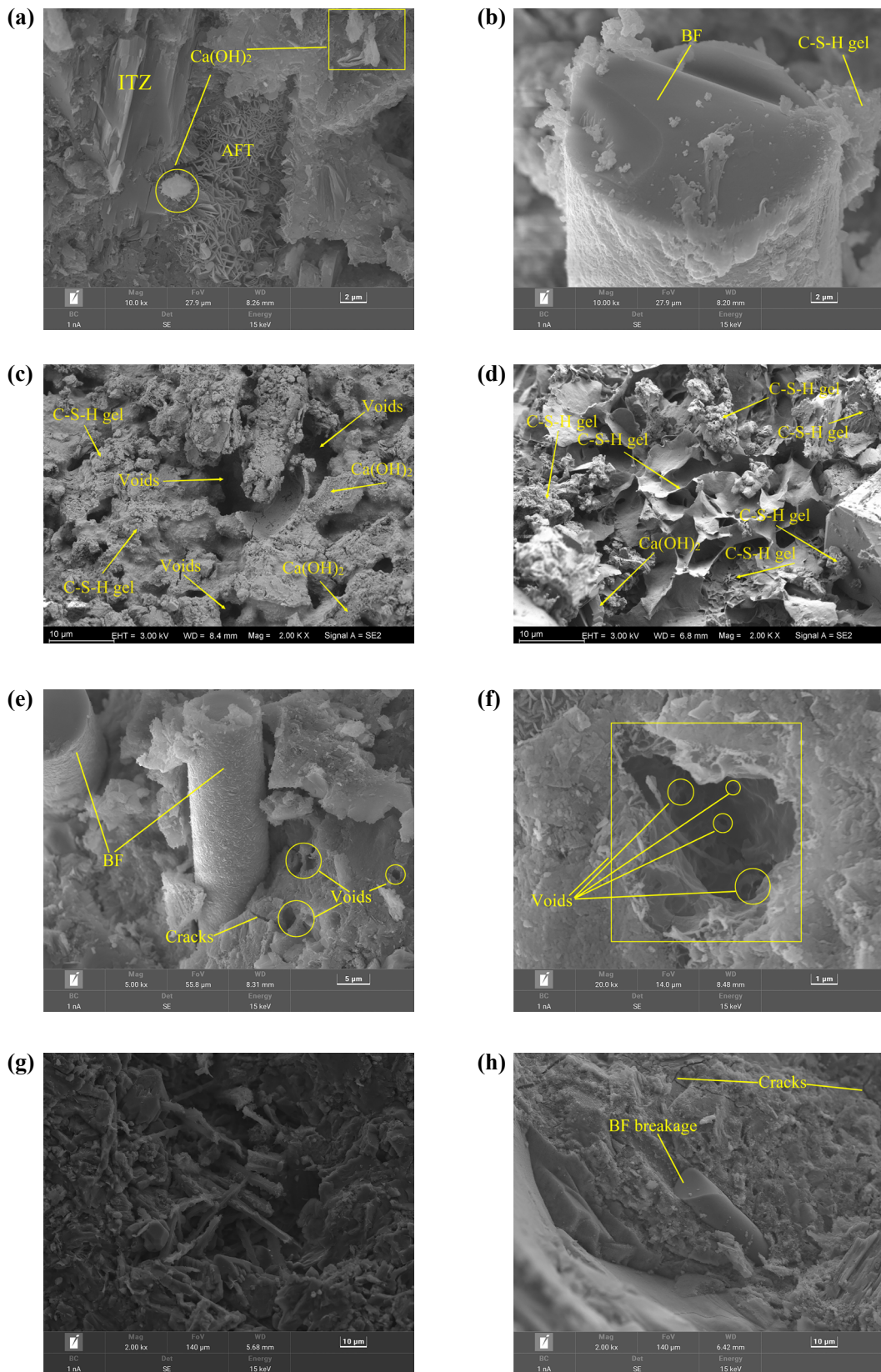


FIGURE 8. SEM images of the concrete in the bonding interface of the BFRP bar. (a) Microstructure of HF after 20 °C; (b) BF after 20 °C; (c) Hydration products of HN after 20 °C; (d) Hydration products of HF after 20 °C; (e) Microstructure of HF after 200 °C; (f) Microstructure of HN after 200 °C; (g) Microstructure of HF after 300 °C; (h) BF-cement paste interface after 300 °C.

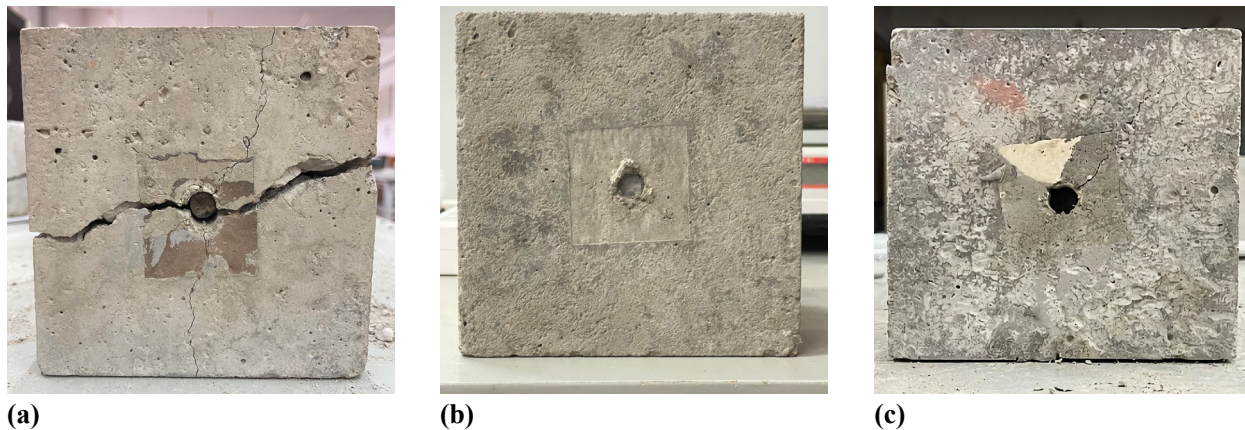


FIGURE 9. Failure modes. (a) Splitting; (b) Pull-out; (c) Pull-out splitting.

Pull-out failure specimens maintained good integrity, as no obvious cracks on the front and side. The bars were gradually pulled out with the increase in load, due to the shear strength of bars being much smaller than the tensile strength of concrete. When the free end was pulled out to a distance of roughly 20 mm, the loading was stopped. All specimens below 300 °C of HN and HF exhibited pull-out failures.

After 300 °C, the HN specimens experienced splitting failure, and the concrete was split into two pieces, whereas the HF specimens experienced pull-out splitting failure. The bars were gradually pulled out as the load increased, and obvious cracks emerged on the specimen surface in pull-out splitting failure, while integrity was preserved.

3.4. Bond strength

3.4.1. Influence of high temperature on bond strength

Table 7 presents the test results of the bond strength, and Figure 10 depicts the variation of bond strength with temperature. As the temperature rose, the bond strength of each group decreased. The bond strength of HN specimens reduced by 9.7 %, 18.0 %, and 27.3 %, respectively, after exposure to 100 °C, 200 °C, and 300 °C, compared with that of HN specimens at 20 °C. Similarly, the bond strength of HF specimens declined by 4.1 %, 11.7 %, and 20.8 %, respectively, compared with that of HF specimens at 20 °C.

For concrete, the free water and capillary water started to gradually evaporate and disappear at 100 °C, which made the porosity of the concrete increase (39), resulting in a gradual decrease of concrete strength, which in turn, affected the bond strength negatively. At 200 °C, the proposition of free and capillary water evaporated increased, and the AFT dehydrated and decomposed, and degradation emerged on the interfacial transition zone (ITZ). At 300 °C, CH thermally

decomposed into CaO, micro-cracks were generated by the thermal expansion of concrete, and the bond deterioration of the ITZ became more severe.

For BFRP bars, the tensile strength deteriorated with the temperature increase, and the deterioration was the most serious at 300 °C. Moreover, the thermal expansion coefficient between bars and concrete was different, tensile stress was generated inside the concrete when the temperature increased, which caused the generation of microcracks. Thus the bond property was influenced (40). Furthermore, the sand particles on the bars' surface fell off with the increase in temperature, and the ribs degraded and became shallow. The mechanical interaction and friction force that provided the bond stress were reduced to different degrees (41). The combined deterioration of concrete and BFRP bars made the bond strength decrease with the increased temperature, and the decrease became more pronounced.

3.4.2. Influence of incorporation of hybrid fiber on bond strength

The bond strength of HF specimens was higher than that of HN specimens after exposure to the same temperature, as it was 16.6 %, 23.9 %, 25.7 %, and 27.1 % higher than that of HN specimens after exposure to 20 °C, 100 °C, 200 °C, and 300 °C, respectively. The incorporation of BF and CF enhanced the bonding durability under high temperatures, and the enhancement effect became more significant as temperature increased.

The randomly distributed BF formed a three-dimensional staggered support network inside the concrete, which could effectively reduce the shrinkage strain and inhibit the expansion of concrete shrinkage cracks (42, 43). Moreover, BF and matrix formed a spatial whole due to the strong bond between them, which increased the bonding force. CF had good hydrophilicity, which could absorb water inside the concrete, reduce the porosity of the concrete, and also play an internal curing

and promotion of hydration role in the concrete (44). The two fibers complemented each other and showed a positive synergistic effect. Therefore, the bond strength and the bonding durability under high temperatures were improved effectively.

High temperatures caused free water to evaporate and migrate along pores and microcracks. The water then reacted with unhydrated particles, which made the hydrate reaction more thorough (45). This process made the cement paste more compact and generated more hydration products on the fibers. Thus the bond between fibers and cement paste strengthened. Moreover, the pores formed by the melting of CF in HF assisted in regulating the matrix’s temperature and lessened internal stress brought on by the temperature gradient. Therefore, the enhancement effect of BF and CF increased when the temperature increased.

3.4.3. Residual bond strength

The incorporation of BF and CF effectively increased the residual bond strength. The test data were used to establish the fitting curves of residual bond strength of HN and HF specimens, as shown in Figure 11. The fitting relationships were given by Equations [2] and [3].

$$\text{HN: } \frac{\tau^T}{\tau^{20}} = 0.99895 - 9.405 \times 10^{-4}T + 1.25 \times 10^{-7}T^2 \quad R^2 = 0.998 \quad [2]$$

$$\text{HF: } \frac{\tau^T}{\tau^{20}} = 1.00075 - 3.525 \times 10^{-4}T - 1.175 \times 10^{-6}T^2 \quad R^2 = 0.999 \quad [3]$$

Where τ^{20} was the bond strength of specimens after exposure to 20 °C, MPa; τ^T was the bond strength of specimens after exposure to high temperature, MPa; T was temperature, °C.

3.5. Bond-slip curve

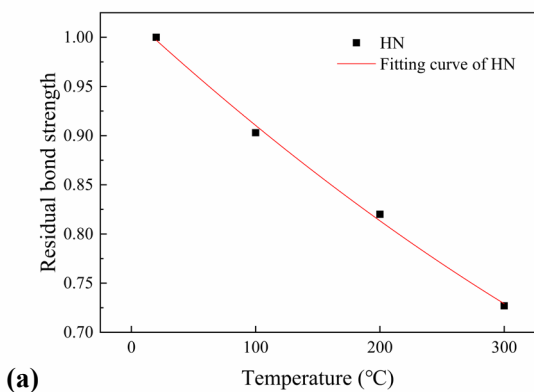


TABLE 7. Pull out test results of BFRP bar and hybrid fiber reinforced concrete.

Specimen number	F (kN)	τ_u (MPa)	S_u (mm)	DR (%)	Failure mode
HN20	48.76	21.57	2.29	/	Pull out
HN100	44.01	19.47	3.10	9.74	Pull out
HN200	39.98	17.68	4.10	18.03	Pull out
HN300	35.45	15.68	5.10	27.31	Splitting
HF20	56.87	25.16	3.05	/	Pull out
HF100	54.55	24.13	3.25	4.09	Pull out
HF200	50.25	22.23	4.45	11.65	Pull out
HF300	45.05	19.93	6.35	20.79	Pull-out splitting

F : Ultimate load; τ_u : Bond strength; S_u : Peak slip value; DR : Decrease rate of bond strength.

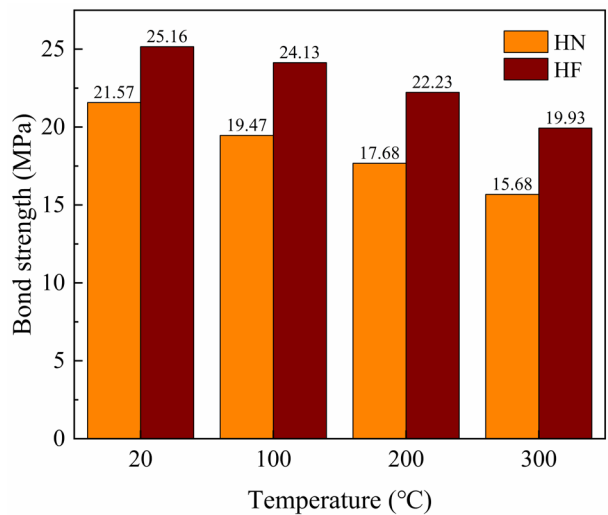


FIGURE 10. Bond strength.

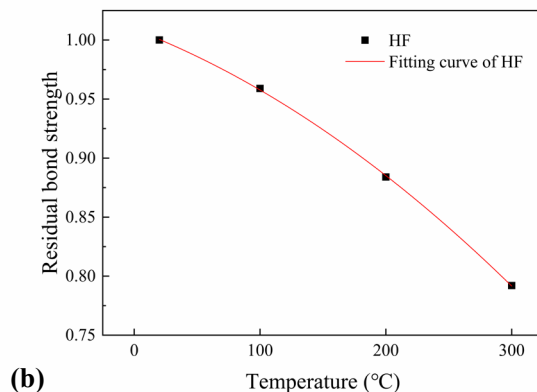


FIGURE 11. Fitting curves of residual bond strength of HN and HF specimens. (a) HN; (b) HF.

Figure 12 shows the bond-slip curves. The change rule of the HN and HF specimens was consistent. The bond stiffness and bond strength of each specimen gradually decreased, and the peak slip increased, with the increase in temperature. Four stages could be divided into the curves: the micro slip stage, the slip stage, the pull-out stage, and the residual stress stage. However, there were only the first three stages on the curve of the splitting failure specimen (HF300). In the beginning, the curve was in the micro slip stage. There were micro slip occurrences on the loading end, and the bond stress increased linearly. The chemical adhesion mainly provided the bond stress. The curve entered the slip stage with the loading continued, where the relative slip began to appear, and the bond stress rose nonlinearly. The chemical adhesive force disappeared, and the mechanical interaction and friction force between the transverse rib of the BFRP bar and the concrete interface mainly provided the bonding force. After the bond stress reached peak value, the curve entered the pull-out stage. Due to the further wear of the ribs of the bars, the concrete between the ribs being cut into pieces, the mechanical interaction weakened sharply, resulting in a gradual decrease in the bond stress. A nonlinear decrease was shown in the bond stress in the residual stress stage. Due to the slow pull-out of BFRP bars, the free end reserved outside entered into the concrete, and the mechanical interaction and friction force between the transverse ribs on the free end and the concrete interface was generated, which made the specimen regain some bonding force.

3.5.1. Influence of high temperature on bond properties

The bond stiffness also decreased as temperature increased. The bond stiffness of HN decreased by 30.4 %, 53.2 %, and 67.5 % at 100 °C, 200 °C, and 300 °C, respectively, while the bond stiffness of HF decreased by 26.9 %, 52.7 %, and 55.0 % at the same temperatures. Figure 13 depicts the variation of bond stiffness with temperature.

The main reason for the above results was that the gradual vitrification, decomposition, and carbonization of matrix resin of BFRP bars with increased temperature, resulting in the gradual decrease of chemical adhesive force, friction force, and mechanical interaction force (46). The specimens after exposure to 200 °C could restore the tensile strength of bars and the bond strength to a certain extent after they were naturally cooled to 20 °C. The polymer resin decomposed after 300 °C, and the tensile strength of the bars decreased significantly, which could not be restored. Hence, high temperature influenced the bond stiffness. Moreover, the extrusion between the transverse rib of the BFRP bar and the concrete produced the oblique force, which produced radial and tangential components and caused the surrounding concrete to be in a circumferential tension state. The bond failure would occur when the circumferential stress exceeded the concrete tensile strength. The temperature increase reduced the concrete tensile strength, which led to premature bond failure, and the bond strength and stiffness also reduced.

3.5.2. Influence of incorporation of hybrid fiber on bond properties

Figure 13 shows that the hybrid fibers significantly improved the bond stiffnesses. The bond stiffness of HF specimens increased by 7.7 %, 13.1 %, 8.8 %, and 49.1 %, respectively, compared with that of HN specimens after exposure to 20 °C, 100 °C, 200 °C, and 300 °C.

The phenomenon had two underlying causes. The first one was the addition of BF and CF, which increased the concrete strength, prevented premature bond failure of specimens, and improved the bond properties. The second one was the CF in the HF specimen promotes hydration, resulting in more hydration products on the bonding surface of the bar, which would enhance the chemical adhesive and mechanical interaction between the BFRP bar and matrix. The chemical adhesive force and mechanical interaction made part of the loading force transfer to the tangen-

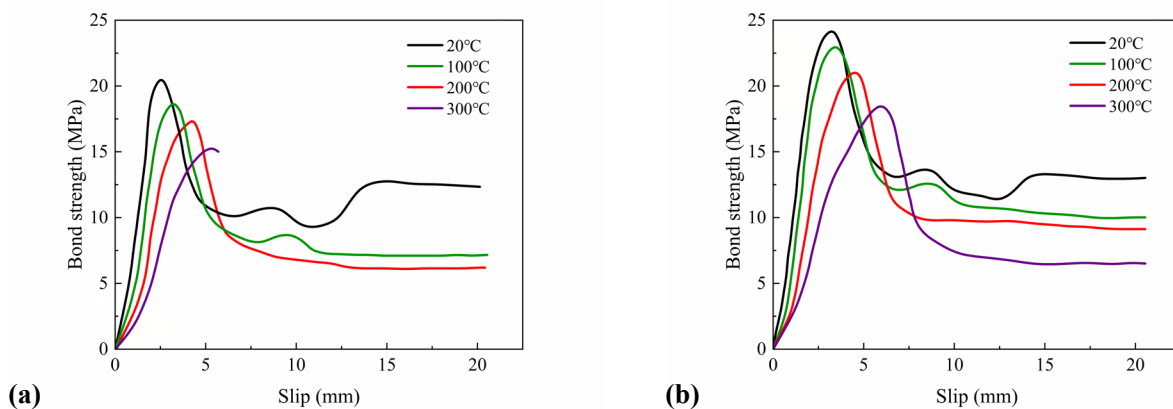


FIGURE 12. Bond-slip curves. (a) HN; (b) HF.

tial direction of the bond area. Thus, the circumferential and radial tensile stresses of HF were smaller than those of HN under the same loading force. This led to a reduction in the cracking speed, and an effective enhancement of the bond properties.

3.6. Bond-slip constitutive model between bfrp bar and concrete after exposure to high temperature

3.6.1. Existing models

Bond properties were the basis of the FRP bars and concrete working together. A lot of research on the bond properties has been done by scholars, and corresponding bond-slip constitutive models have been proposed. The function expressions of each model are shown in Table 8.

One of them was the Malvar model, which was proposed in 1994 by Malvar (47) after studying the influences of three different GFRP bars on bond strength. The axisymmetrical radial pressure σ_r was

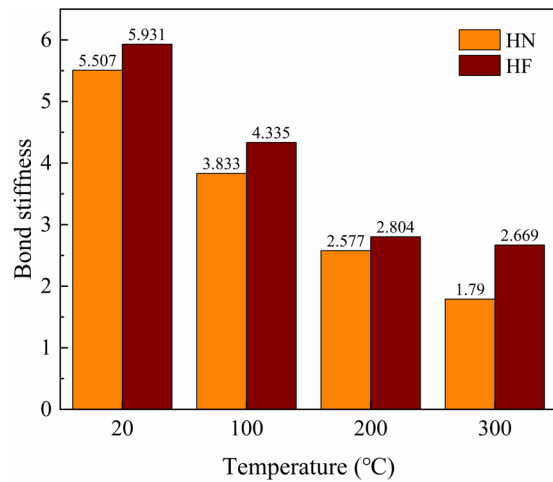


FIGURE 13. Bond stiffness.

introduced, and the peak bond strength τ_i and the peak slip s_i defined the functional expression of σ_r . A subsequent model was the BPE model, which was proposed by Eligehausen et al. (48) in 1983 to describe

TABLE 8. Bond-slip constitutive models.

Constitutive model	Function expressions
Malvar model	$\tau_1/f_t = A + B(1 - e^{C\sigma_r/f_t}); s_1 = D + E\sigma_r;$ $\tau/\tau_1 = \frac{F(s/s_1) + (G - 1)(s/s_1)^2}{1 + (F - 2)(s/s_1) + (G - 1)(s/s_1)}$
BPE model	$\tau/\tau_1 = (s/s_1)^\alpha, (s \leq s_1)$ $\tau = \tau_1, (s_1 < s \leq s_2)$ $\tau = \tau_1 - \frac{\tau_1 - \tau_3}{s_2 - s_3}(s_2 - s), (s_2 < s \leq s_3)$ $\tau = \tau_3 (s > s_3)$
MBPE model	$\tau/\tau_1 = (s/s_1)^\alpha, (s \leq s_1);$ $\tau = [1 - p(s/s_1 - 1)]\tau_1, (s_1 < s \leq s_3);$ $\tau = \tau_3, (s > s_3)$
CMR model	$\tau = (1 - e^{-s/s_r})^\beta \tau_1$
Continuous curve model	$\tau = \left(2\sqrt{s/s_1} - \frac{s}{s_1}\right) \tau_1, (0 < s \leq s_1);$ $\tau = \frac{\tau_1(s_3 - s)^2(2s + s_3 - s_1)}{(s_3 - s_1)^3} + \frac{\tau_3(s - s_1)^2(3s_3 - 2s - s_1)}{(s_3 - s_1)^3}, (s_1 < s \leq s_3);$ $\tau = \tau_3, (s > s_3)$

σ_r : Axisymmetrical radial pressure; f_t : Tensile strength of concrete; τ, s_i : Bond strength and peak slip; τ_3, s_3 : Residual strength and corresponding slip; $A, B, C, D, E, F, G, \alpha, \beta, s_2, s_r$: Parameters determined by test results.

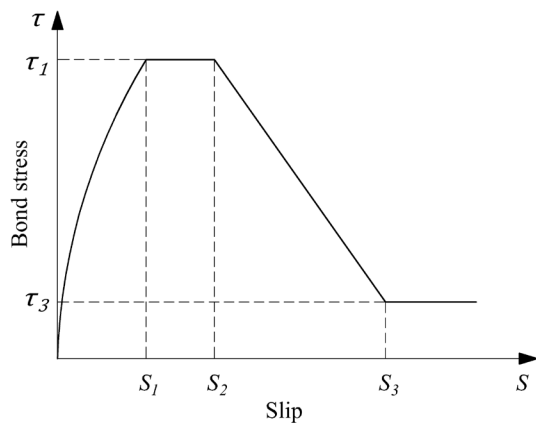


FIGURE 14. BPE model.

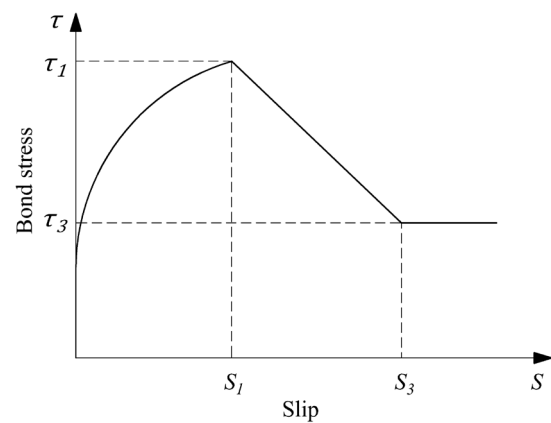


FIGURE 15. MBPE model.

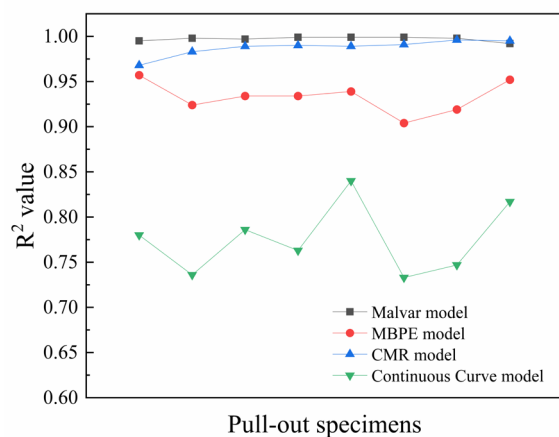
the bond-slip curve of deformed steel bars. The BPE model was successfully applied by Cosenza et al. (49) to the analysis of FRP bars reinforced concrete structures. In this model, the curve was divided into 4 stages: an ascending stage, a horizontal stage, a descending stage, and a residual stage, as shown in Figure 14. Since there was no horizontal stage in practical engineering, in 1996, Cosenza et al. (50) considered the actual situation. They improved the horizontal stage in the BPE model, namely the MBPE model, which is shown in Figure 15. Furthermore, it has been discovered that only the rising section of the curve needs to be considered in most structural calculations. Thus Cosenza et al. (51) proposed CMR model that could describe the rising section more accurately. For the purpose of making the bond-slip curve smoother and more continuous, Gao et al. (52) introduced four parameters to modify the existing model and proposed a mathematical model of a constant curve.

3.6.2. Bond-slip constitutive models comparison

To achieve a more scientific and standardized application of FRP bar hybrid fiber reinforced concrete structure, using the Malvar, MBPE, CMR, and Continuous Curve models to fit ascending sections of bond-slip curves obtained from this test through Origin software, and the results were compared to verify the models. The comparison of the average coefficient of determination (average R^2 values) of each model obtained by fitting is shown in Figure 16. The average R^2 values of the Malvar, MBPE, CMR, and Continuous Curve models obtained by fitting were 0.997, 0.933, 0.988, and 0.775, respectively. It could be seen that the Malvar, CMR, and MBPE models could all fit the ascending sections of the curves accurately. The fitting effect of the Malvar model was the best, and the fitting effect of the CMR model was very close to the Malvar model, but slightly worse than the Malvar model. Although the MBPE model was worse than the Malvar model and CMR model, the R^2 val-

ues obtained by fitting the curves of each specimen were all above 0.9, which there was still a good fitting effect. The Continuous Curve model was the worst. Figures 17 and 18 show that the fluctuation of the fitting effect of each model on the ascending sections of HF was larger than that of HN. There was the same variation trend on the fitting effect of each model on HF as that of HN with the temperature increased from 20 °C to 200 °C.

Regarding the descending sections, using the Malvar, MBPE, and Continuous Curve models to fit them.

FIGURE 16. Comparison of R^2 values on ascending section.

The comparison of the fitting effects of each model is shown in Figure 19. The average R^2 values obtained from the Malvar, MBPE, and Continuous Curve models fitting the descending sections of the test curves for each specimen were 0.912, 0.952, and 0.978, respectively. The situation was different from that of fitting the ascending section, the Continuous Curve model was the best when fitting the descending section, and the MBPE model was slightly worse. The Malvar model was the worst, and it fluctuated signif-

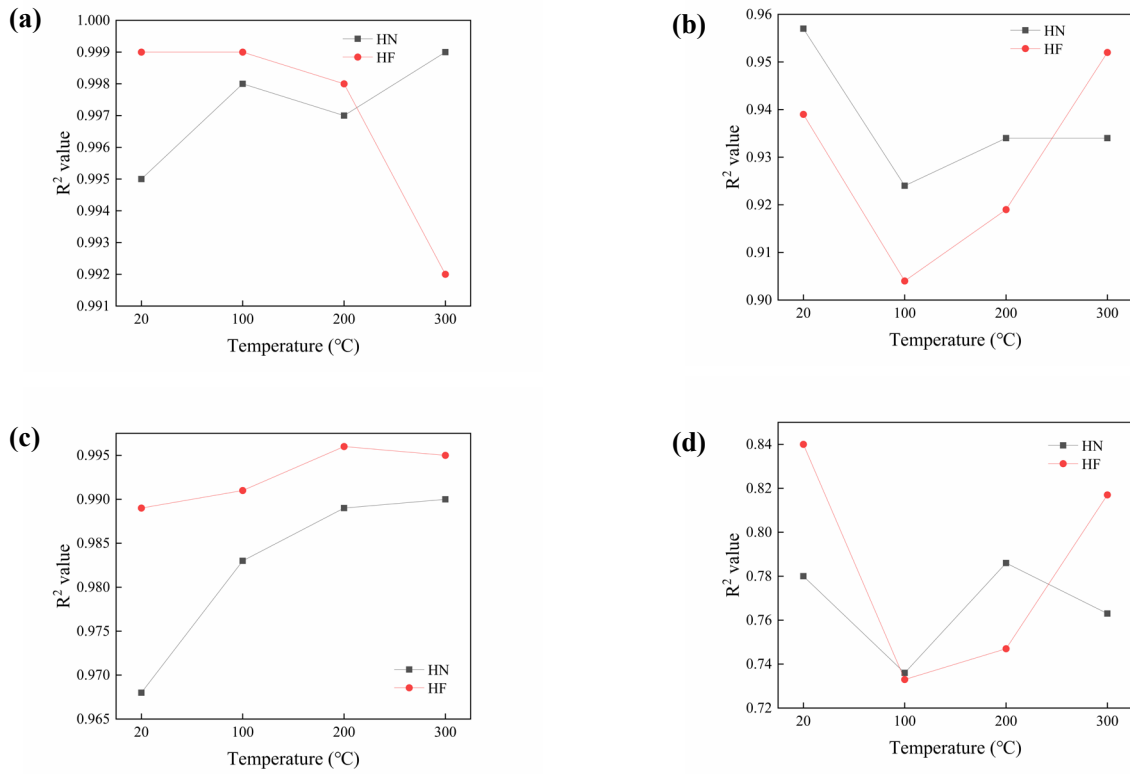


FIGURE 17. (a) R^2 values for the Malvar model fitting the ascending section; (b) R^2 values for the MBPE model fitting the ascending section; (c) R^2 values for the CMR model fitting the ascending section; (d) R^2 values for the Continuous Curve model fitting the ascending section.

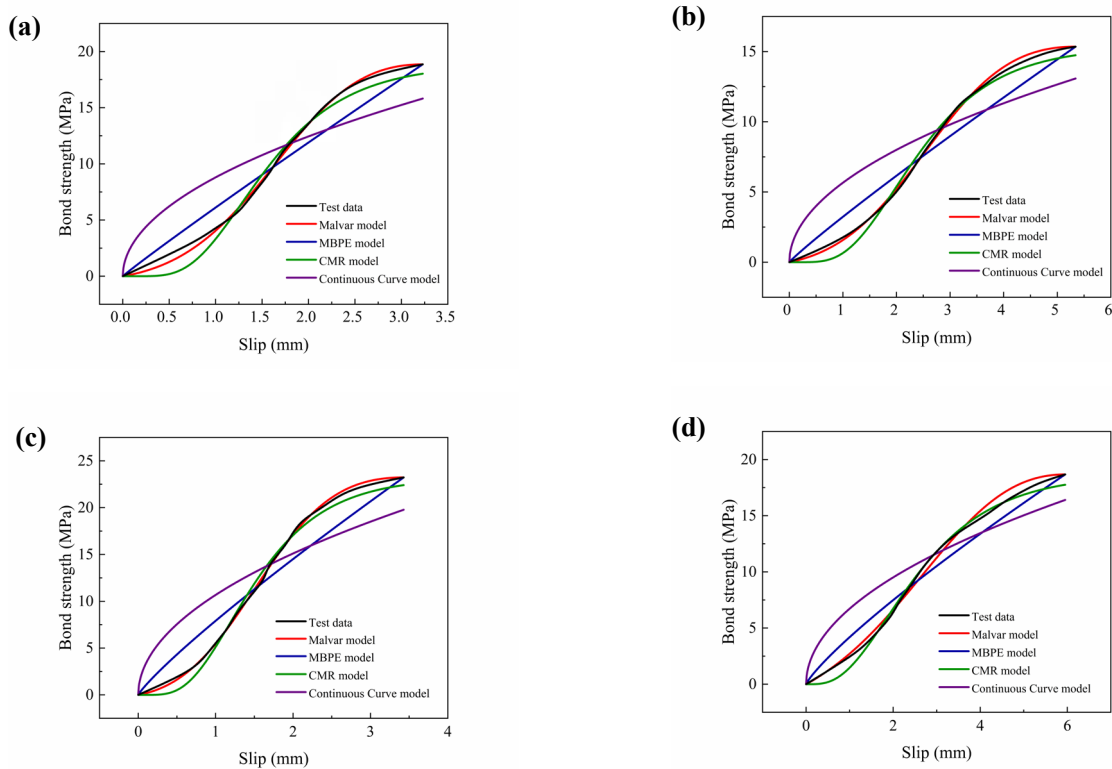


FIGURE 18. Comparison of curves of each model fitting ascending section. (a) HN100; (b) HN300; (c) HF100; (d) HF300.

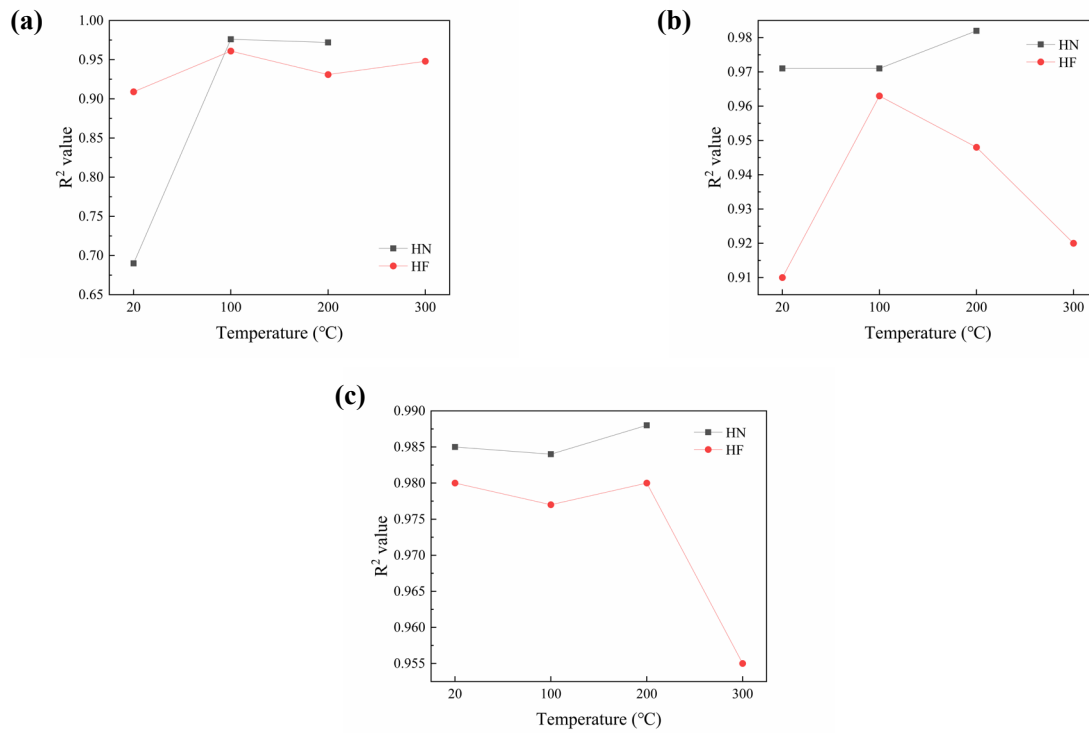


FIGURE 20. (a) R^2 values for the Malvar model fitting the descending section; (b) R^2 values for the MBPE model fitting the descending section; (c) R^2 values for the Continuous Curve model fitting the descending section.

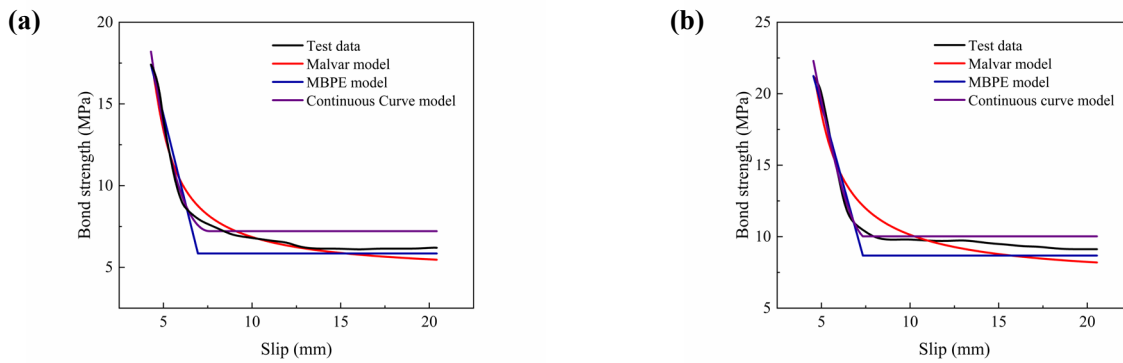


FIGURE 21. Comparison of curves of each model fitting descending section. (a) HN200; (b) HF200.

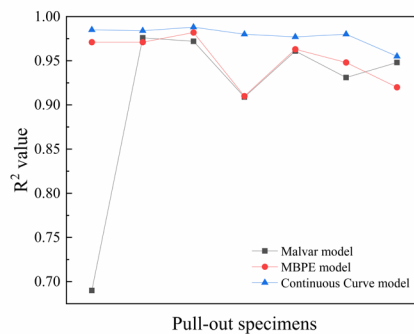


FIGURE 19. Comparison of R^2 values on descending section.

icantly. It did not show the same good effect as that of fitting the ascending sections. Figure 20 and Figure 21 show that the fitting effects of each model on the descending sections of HN were better than that of HF. Similarly, there was still the same variation trend on the fitting effect of the Malvar model and Continuous Curve model on HF as that of HN with the temperature increased from 20 °C to 200 °C.

4. CONCLUSIONS

This paper presented an experiment and theoretical analysis of HN and HF pull-out specimens that have been cooled to 20 °C after being subjected to high-temperature treatment at different temperatures. The main conclusions are as follows:

1. As the temperature increased, a reduction was exhibited in the tensile strength of BFRP bars, a change in surface color to black, and a loss of sand particles. Specifically, exposure to 300 °C resulted in a significant 41.8 % decrease in the tensile strength, and exposure to 400 °C further reduced it to a mere 13.2 % of its original strength at 20 °C.
2. The BF with a high melting point created a strong bond with the matrix, effectively preventing crack propagation. On the other hand, the low melting point CF melted, leaving pores and channels in the matrix. This helped to reduce thermal stress and temperature gradients within and across the concrete. The synergistic effect of these two types of fibers led to an improved microstructure.
3. When exposure temperatures were lower than 300 °C, all specimens failed by pull-out. However, at higher than 300 °C, the failure modes changed to splitting for HN specimens and pull-out splitting for HF specimens.
4. The bond stiffness and strength decreased with increasing temperature. The maximum reductions observed were 27.3 % and 20.8 % for bond strength, and 67.5 % and 55.0 % for bond stiffness of HN and HF pull-out specimens, respectively. The bond strength and stiffness of HF specimens were 27.1 % and 49.1 % higher, respectively, than those of the HN specimens at the same temperature. The polynomial fitting of the residual bond strength showed good results.
5. The Malvar model fitted the ascending section best, and the fit quality of each model varied more for the HF curve than the HN curve. The Continuous Curve model fitted the descending section best, and the fit quality of each model was better for the HN curves than the HF curves.

Funding Sources

Research carried out within the framework of Grant No. Y202146776, financed by the Zhejiang Province De-

partment of Education Fund; Grant No. JYL201915404, financed by the Natural Science Foundation Project of Liaoning Provincial Department of Education, China and Grant No. LQ22E080024 financed by the Zhejiang Provincial Natural Science Foundation of China.

Authorship contribution statement

Zhenrong Liu: Conceptualization, Formal analysis, Methodology, Validation, Visualization, Writing, original draft, Writing, review & editing.

Huaxin Liu: Data curation, Funding acquisition, Validation, Writing, review & editing.

Weixing Xu: Investigation, Project administration.

Beibei Liu: Investigation, Project administration, Writing, review & editing.

Yue Zhong: Resources.

Jian Geng: Software.

Genjin Liu: Formal analysis, Funding acquisition, Writing, review & editing.

The authors of this article declare that they have no financial, professional or personal conflicts of interest that could have inappropriately influenced this work.

REFERENCES

1. Amran M, Murali G, Makul N, Kurpińska M, Nehdi ML. 2023. Fire-induced spalling of ultra-high performance concrete: A systematic critical review. *Constr. Build. Mater.* 373:130869. <https://doi.org/10.1016/j.conbuildmat.2023.130869>.
2. Kiran T, Yadav SK, Anand N, Mathews ME, Andrushia D, Lubloy E, Kodur V. 2022. Performance evaluation of lightweight insulating plaster for enhancing the fire endurance of high strength structural concrete. *J. Build. Eng.* 57:104902. <https://doi.org/10.1016/j.job.2022.104902>.
3. Miah MJ, Lo Monte F, Felicetti R, Pimienta P, Carré H, La Borderie C. 2023. Impact of external biaxial compressive loading on the fire spalling behavior of normal-strength concrete. *Constr. Build. Mater.* 366:130264. <https://doi.org/10.1016/j.conbuildmat.2022.130264>.
4. Asghari Ghajari F, Yousefpour H. 2023. Cyclic bond behavior in reinforced concrete flexural members exposed to elevated temperatures. *Eng. Struct.* 292:116520. <https://doi.org/10.1016/j.engstruct.2023.116520>.
5. Ahmad S, Rasul M, Adekunle SK, Al-Dulaijan SU, Maslehuddin M, Ali SI. 2019. Mechanical properties of steel fiber-reinforced UHPC mixtures exposed to elevated temperature: Effects of exposure duration and fiber content. *Compos. Part B.* 168:291-301. <https://doi.org/10.1016/j.compositesb.2018.12.083>.
6. Eidan J, Rasoolan I, Rezaeian A, Poorveis D. 2019. Residual mechanical properties of polypropylene fiber-reinforced concrete after heating. *Constr. Build. Mater.* 198:195-206. <https://doi.org/10.1016/j.conbuildmat.2018.11.209>.
7. Vafaei D, Ma X, Hassanli R, Duan J, Zhuge Y. 2022. Microstructural and mechanical properties of fiber-reinforced seawater sea-sand concrete under elevated temperatures. *J. Build. Eng.* 50:104140. <https://doi.org/10.1016/j.job.2022.104140>.
8. Zhao C, Zhu Z, Guo Q, Zhan Y, Zhao R. 2023. Research on fiber reinforced concrete and its performance prediction method and mix design method. *Constr. Build. Mater.* 365:130033. <https://doi.org/10.1016/j.conbuildmat.2022.130033>.
9. Cao M, Li L, Khan M. 2018. Effect of hybrid fibers, calcium carbonate whisker and coarse sand on mechanical properties of cement-based composites. *Mater. Construcc.* 68(330):e156. <https://doi.org/10.3989/mc.2018.01717>.

10. Li L, Cao M, Li Z, Zhang W, Shi D, Shi K. 2022. Uniaxial tensile behavior and mechanism characterization of multi-scale fiber-reinforced cementitious materials. *Mater. Construcc.* 72(345):e271. <https://doi.org/10.3989/mc.2022.05521>.
11. Fu Q, Xu W, Bu M, Guo B, Niu D. 2021. Effect and action mechanism of fibers on mechanical behavior of hybrid basalt-polypropylene fiber-reinforced concrete. *Structures.* 34:3596-3610. <https://doi.org/10.1016/j.istruc.2021.09.097>.
12. Zhu M, Qiu J, Chen J. 2022. Effect and mechanism of coal gangue concrete modification by basalt fiber. *Constr. Build. Mater.* 328:126601. <https://doi.org/10.1016/j.conbuildmat.2022.126601>.
13. Sun J, Ding Z, Li X, Wang Z. 2021. Bond behavior between BFRP bar and basalt fiber reinforced seawater sea-sand recycled aggregate concrete. *Constr. Build. Mater.* 285:122951. <https://doi.org/10.1016/j.conbuildmat.2021.122951>.
14. Patel N, Patel K, Gohil P, Chaudhry V. 2018. Investigations on mechanical strength of hybrid basalt/glass polyester composites. *Int. J. Appl. Eng. Res.* 13(6):4083-4088.
15. Hassani Niaki M, Fereidoon A, Ghorbanzadeh Ahangari M. 2018. Experimental study on the mechanical and thermal properties of basalt fiber and nanoclay reinforced polymer concrete. *Compos. Struct.* 191:231-238. <https://doi.org/10.1016/j.compstruct.2018.02.063>.
16. Ren W, Xu J, Su H. 2016. Dynamic compressive behavior of basalt fiber reinforced concrete after exposure to elevated temperatures. *Fire Mater.* 40(5):738-755. <https://doi.org/10.1002/fam.2339>.
17. Ardanuy M, Claramunt J, Toledo Filho, RD. 2015. Cellulosic fiber reinforced cement-based composites: A review of recent research. *Constr. Build. Mater.* 79:115-128. <https://doi.org/10.1016/j.conbuildmat.2015.01.035>.
18. Chami Khazraji A, Robert S. 2013. Self-assembly and intermolecular forces when cellulose and water interact using molecular modeling. *J. Nanomater.* 2013:745979. <https://doi.org/10.1155/2013/745979>.
19. Soroushian P, Won JP, Hassan M. 2012. Durability characteristics of CO₂-cured cellulose fiber reinforced cement composites. *Constr. Build. Mater.* 34:44-53. <https://doi.org/10.1016/j.conbuildmat.2012.02.016>.
20. Hisseine OA, Wilson W, Sorelli L, Tolnai B, Tagnit-Hamou A. 2019. Nanocellulose for improved concrete performance: A macro-to-micro investigation for disclosing the effects of cellulose filaments on strength of cement systems. *Constr. Build. Mater.* 206:84-96. <https://doi.org/10.1016/j.conbuildmat.2019.02.042>.
21. Chen L, Su RKL. 2022. On the corrosion rate measurement of reinforcing steel in chloride induced macrocell corrosion. *Cem. Concr. Compos.* 134:104775. <https://doi.org/10.1016/j.cemconcomp.2022.104775>.
22. Wang Q, Zhu H, Teng F, Li H. 2023. Experimental and analytical studies of the bond between ribbed CFRP bar and aluminum alloy additional ribs anchorage. *Eng. Fract. Mech.* 290:109504. <https://doi.org/10.1016/j.engfracmech.2023.109504>.
23. Jiang Z, Fang Z, Fang C, Li Q, Wang Z. 2022. Mechanical properties under high-temperature and fire resistant limit of carbon fiber reinforced polymer cable. *Constr. Build. Mater.* 361:129586. <https://doi.org/10.1016/j.conbuildmat.2022.129586>.
24. Hajiloo H, Green MF. 2018. Bond strength of GFRP reinforcing bars at high temperatures with implications for performance in fire. *J. Compos. Constr.* 22(6):04018055. [https://doi.org/doi:10.1061/\(ASCE\)CC.1943-5614.0000897](https://doi.org/doi:10.1061/(ASCE)CC.1943-5614.0000897).
25. Hamad RJA, Megat Johari MA, Haddad RH. 2017. Mechanical properties and bond characteristics of different fiber reinforced polymer rebars at elevated temperatures. *Constr. Build. Mater.* 142:521-535. <https://doi.org/10.1016/j.conbuildmat.2017.03.113>.
26. Li C, Gao D, Wang Y, Tang J. 2017. Effect of high temperature on the bond performance between basalt fibre reinforced polymer (BFRP) bars and concrete. *Constr. Build. Mater.* 141:44-51. <https://doi.org/10.1016/j.conbuildmat.2017.02.125>.
27. Shaikh FUA. 2018. Mechanical properties of concrete containing recycled coarse aggregate at and after exposure to elevated temperatures. *Struct. Concr.* 19(2):400-410. <https://doi.org/10.1002/suco.201700084>.
28. GB/T 14685-2022. 2022. Pebble and crushed stone for construction. *Chin. Stand.*
29. GB/T 14684-2022. 2022. Sand for construction. *Chin. Stand.*
30. JGJ 55-2011. 2011. Specification for Mix proportion design of ordinary concrete. *Chin. Stand.*
31. Zhu B. 2021. Experimental study on the bond behavior between BFRP bars and recycled aggregate concrete. Master thesis. Liaoning University of Technology.
32. Xu H, Shao Z, Wang Z, Cai L, Li Z, Jin H, Chen T. 2020. Experimental study on mechanical properties of fiber reinforced concrete: Effect of cellulose fiber, polyvinyl alcohol fiber and polyolefin fiber. *Constr. Build. Mater.* 261:120610. <https://doi.org/10.1016/j.conbuildmat.2020.120610>.
33. Committee ACI. 2012. ACI 440.3 R-12 Guide for test methods for fiber reinforced polymers (FRP) for reinforcing and strengthening concrete structures.
34. Committee ACI. 2006. ACI 440.1 R-06 Guide for the design and construction of structural concrete reinforced with FRP bars.
35. Nepomuceno E, Sena-Cruz J, Correia L, D'Antino T. 2021. Review on the bond behavior and durability of FRP bars to concrete. *Constr. Build. Mater.* 287:123042. <https://doi.org/10.1016/j.conbuildmat.2021.123042>.
36. GB/T 30022-2013. 2013. Test method for basic mechanical properties of fiber reinforced polymer bar. *chin. stand.*
37. ASTM D7913/D7913M-14. 2014. Bond strength of fiber-reinforced polymer matrix composite bars to concrete by pullout testing. *ASTM Stand.*
38. Khaneghahi MH, Ghamsari AK, Ozbakkaloglu T. 2021. Stress-relaxation behavior of fiber-reinforced polymer sheets at elevated temperatures. *Constr. Build. Mater.* 307:124900. <https://doi.org/10.1016/j.conbuildmat.2021.124900>.
39. Shen J, Xu Q. 2019. Effect of elevated temperatures on compressive strength of concrete. *Constr. Build. Mater.* 229:116846. <https://doi.org/10.1016/j.conbuildmat.2019.116846>.
40. Bilotta A, Compagnone A, Esposito L, Nigro E. 2020. Structural behaviour of FRP reinforced concrete slabs in fire. *Eng. Struct.* 221:111058. <https://doi.org/10.1016/j.engstruct.2020.111058>.
41. Katz A, Berman N, Bank LC. 1999. Effect of high temperature on bond strength of FRP rebars. *J. Compos. Constr.* 3(2):73-81. [https://doi.org/doi:10.1061/\(ASCE\)1090-0268\(1999\)3:2\(73\)](https://doi.org/doi:10.1061/(ASCE)1090-0268(1999)3:2(73)).
42. Dong JF, Wang QY, Guan Z. W. 2017. Material properties of basalt fibre reinforced concrete made with recycled earthquake waste. *Constr. Build. Mater.* 130:241-251. <https://doi.org/10.1016/j.conbuildmat.2016.08.118>.
43. Wang Y, Hughes P, Niu H, Fan Y. 2019. A new method to improve the properties of recycled aggregate concrete: Composite addition of basalt fiber and nano-silica. *J. Cleaner Prod.* 236:117602. <https://doi.org/10.1016/j.jclepro.2019.07.077>.
44. Liu J, Lv C. 2021. Research progress on durability of cellulose fiber-reinforced cement-based composites. *Int. J. Polym. Sci.* 2021:1014531. <https://doi.org/10.1155/2021/1014531>.
45. Akbar A, Liew KM. 2020. Influence of elevated temperature on the microstructure and mechanical performance of cement composites reinforced with recycled carbon fibers. *Composites Part B.* 198:108245. <https://doi.org/10.1016/j.compositesb.2020.108245>.
46. Alsayed S, Al-Salloum Y, Almusallam T, El-Gamal S, Aqel M. 2012. Performance of glass fiber reinforced polymer bars under elevated temperatures. *Composites Part B.* 43(5):2265-2271. <https://doi.org/10.1016/j.compositesb.2012.01.034>.
47. Malvar, L. J. 1994. Bond stress-slip characteristics of FRP rebars. Port Hueneme, CA, USA: Naval Facilities Engineering Service Center.
48. Eligehausen R, Popov EP, Bertero VV. 1982. Local bond stress slip relationship of deformed bars under generalized excitations. *Calif. The Univ.*
49. Cosenza E, Manfredi G, Realfonzo R. 1995. Analytical modelling of bond between FRP reinforcing bars and concrete. In *Non-metallic (FRP) reinforcement for concrete structures: proceedings of the second international RILEM symposium.* 29:164. CRC Press.
50. Cosenza E, Manfredi G, Realfonzo R. 1996. Bond characteristics and anchorage length of FRP rebars. *Adv. Compos. Mater. Bridges Struct.* 909-916.
51. Cosenza E, Manfredi G, Realfonzo R. 1997. Behavior and modeling of bond of FRP rebars to concrete. *J. Compos. Constr.* 1(2):40-51. [https://doi.org/doi:10.1061/\(ASCE\)1090-0268\(1997\)1:2\(40\)](https://doi.org/doi:10.1061/(ASCE)1090-0268(1997)1:2(40)).
52. Gao D, Zhu H, Xie J. 2003. The constitutive models for bond slip relation between FRP rebars and concrete. *Ind. Constr.* 07:41-43+82.